Exploring stereographic surface energy maps of cubic metals via an effective pair-potential approach

Su-Hyun Yoo,[1,2] Ji-Hwan Lee,[1] Young-Kwang Jung,[1] and Aloysius Soon[1,3,*]

[1]*Global E[3] Institute and Department of Materials Science and Engineering, Yonsei University, 120-749 Seoul, Korea*

[2]*Department of Computational Materials Design, Max-Planck-Insitut für Eisenforschung GmbH, Max-Planck-Str. 1, D-40237 Düsseldorf, Germany*

[3]*School of Physics, University of Sydney, 2006 NSW, Australia*

(Received 7 August 2015; revised manuscript received 17 November 2015; published 20 January 2016)

A fast and efficient way to calculate and generate an accurate surface energy database (of more than several million surface energy data points) for all bcc and fcc metals is proposed based on an effective pair-wise-potential model. The accuracy of this model is rigorously tested and verified by employing density functional theory calculations, which shows good agreement within a mean absolute error of 0.03 eV/atom. The surface energy database generated by this model is then visualized and mapped in various ways; namely, the surface energy as a function of relative orientation, a orientation-dependent stereographic projection (the so-called Wulff net), and Gibbs–Wulff construction of the equilibrium crystal shape, for comparison and analysis. The Wulff nets (drawn with several million surface energy data points) provide us with characteristic surface energy maps of these cubic metals. In an attempt to explain the surface energy anomaly in bcc Li, we demonstrate how our effective-pair-potential-derived Wulff net can clearly discriminate the strong influence of the second- and third-nearest-neighbor bonds on the high-Miller-index surface energetics of bcc Li.

DOI: 10.1103/PhysRevB.93.035434

I. INTRODUCTION

The surface energy γ of a solid is a basic yet central physical quantity of paramount importance and influences many important physico-chemical processes such as interface adhesion, heterogeneous industrial catalysis, oxidative corrosion, and shape-controlled crystal growth. However, direct experimental measurements of these anisotropic surface energies are nontrivial and are also subject to experimental uncertainties such as the presence of impurities [1,2].

In view of the difficulties in obtaining experimental surface energies, including their orientation dependence, accurate electronic-structure calculations based on first-principles density functional theory (DFT) using the (semi) local approximations to the exchange-correlation (xc) functional are typically employed. These studies may indeed have provided an understanding of qualitative trends of surface energies [3–5]. However, most of these studies have largely focused on the study of atomically flat low-Miller-index surfaces. A simple, systematic, yet accurate approach to study the stability of these vicinal metal surfaces (of any surface orientation) is still computationally challenging and not easily attainable.

In essence, γ is the energy cost of making a surface from the corresponding bulk system by cutting chemical bonds as defined by the surface orientation. Thus, a possible starting point is the following simple expression that relates the surface energy as a function of coordination numbers of surface and bulk atoms: $\gamma = (1 - \sqrt{C_S/C_B})E_{coh}$ where C_B and C_S are the full coordination number in the bulk and the local coordination number of surface atoms, respectively, and E_{coh} is the bulk cohesive energy [6,7].

This overly simplified expression only considers the surface energy as a function of the cohesive energy of the metal atoms and its nearest-neighbor bonds. Alternatively, Galanakis *et al.* proposed that γ could also be predicted by using the concept of surface anisotropy ratio—i.e., the ratio of the surface energy of interest to that of the most stable surface [e.g., $\gamma(hkl)/\gamma(111)$ for fcc] [8,9].

A step further was taken by Da Silva *et al.* by using an effective pair-potential (EPP) model (see Refs. [10–12]) to calculate the surface energies of fifteen Cu surfaces [13]. The EPP model is based on a pair-wise expansion of the energy and takes the following form: $\gamma(hkl) = \sum_{s=1}^{S} N_s(hkl)V_s$, where $N_s(hkl)$ is taken as the number of broken bonds in the sth coordination shell for the (hkl) surface, S is the number of coordination shells to be included in the expansion, and V_s is the sth coordination-shell-dependent EPP parameter.

Thus, importantly, one of the main aims of this work is to predict an accurate yet tractable analytical surface energy for thirteen bcc and eleven fcc metals by using DFT energies as *ab initio* input. This affords a fast and efficient recipe for high-throughput calculations of surface energetics of virtually any orientation, requiring only a minimum input of DFT-calculated low-Miller-index surface energies. We further employ cartographic methods to stereographically project these predicted surface energies onto so-called Wulff nets composed of several million surface energies to provide characteristic maps of cubic metals.

II. METHODOLOGY

A. Effective pair potential

Here, we outline the numerical approach for the calculation of the number of broken bonds of plane (hkl), $N(hkl)$, as suggested by Mackenzie *et al.* [15]. According to this model, the bond vectors of an atom in a crystal are defined as $\boldsymbol{u}$. When a plane (hkl) is cleaved, broken and unbroken bonds of the atom located at the surface are determined by a dot product

*aloysius.soon@yonsei.ac.kr

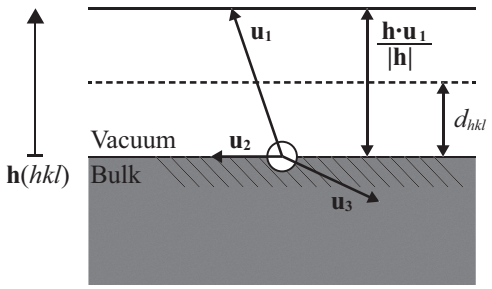

FIG. 1. A schematic figure of a geometrical surface system with the plane (hkl) and the possible bond vectors, $\boldsymbol{u}$ bonds. Here, $\boldsymbol{u}_1$ bond is considered to be a broken bond ($\boldsymbol{h}\cdot\boldsymbol{u}_i > 0$), while $\boldsymbol{u}_2$ and $\boldsymbol{u}_3$ bonds are unbroken ($\boldsymbol{h}\cdot\boldsymbol{u}_i \leqslant 0$). d_{hkl} denotes the spacing between adjacent planes (hkl). The general scheme is adapted from Fig. 1 of Ref. [14].

between the normal vector of the plane, $\boldsymbol{h}$, and each bond vector $\boldsymbol{u}_i$ $(i = 1,2,3,\ldots)$, among $\boldsymbol{u}$ as illustrated in Fig. 1. The bond of $\boldsymbol{u}_i$ is broken if $\boldsymbol{h}\cdot\boldsymbol{u}_i > 0$. Otherwise, the bond remains intact.

Following Ref. [14], the density of broken bonds per area of surface (hkl), $n(hkl)$, is written as

$$n(hkl) = \frac{\sum \boldsymbol{h}\cdot\boldsymbol{u}_i}{|\boldsymbol{h}|\boldsymbol{\Omega}}, \text{ when } \boldsymbol{h}\cdot\boldsymbol{u}_i > 0, \tag{1}$$

where $\boldsymbol{\Omega}$ indicates the volume per atom of the system. Next, the number of broken $\boldsymbol{u}$ bonds per primitive unit cell, $N(hkl)$, can be given by

$$N(hkl) = n(hkl)s(hkl), \text{ when } \boldsymbol{h}\cdot\boldsymbol{u}_i > 0, \tag{2}$$

where $s(hkl)$ is the area of the primitive unit cell of surface.

In crystal systems, $s(hkl)$ can be defined depending on the plane (hkl). In other words, in case of fcc, for instance, when each component, h,k, and l, are all odd, $s(hkl) = 2\boldsymbol{\Omega}|\boldsymbol{h}|$ and otherwise, $s(hkl) = \boldsymbol{\Omega}|\boldsymbol{h}|$. In the similar sense, bcc metals have the surface area of either $2\boldsymbol{\Omega}|\boldsymbol{h}|$ when $h+k+l$ is odd or $\boldsymbol{\Omega}|\boldsymbol{h}|$ when $h+k+l$ is even. Therefore, the number of broken $\boldsymbol{u}$ bonds in the primitive unit cell of the fcc and bcc crystal, $\boldsymbol{N}(hkl)$, at any arbitrary surface can be simplified as follows:

$$N^{\text{fcc}}(hkl) = \frac{3+(-1)^{h\cdot k\cdot l}}{2}\sum \boldsymbol{h}\cdot\boldsymbol{u}_i, \text{ and}$$
$$N^{\text{bcc}}(hkl) = \frac{3-(-1)^{h+k+l}}{2}\sum \boldsymbol{h}\cdot\boldsymbol{u}_i, \text{ when } \boldsymbol{h}\cdot\boldsymbol{u}_i > 0. \tag{3}$$

Based on a simple broken-bond model, the surface energy of plane is calculated by a product between the strength of the first bond and the number of first broken bonds. In the same context, the surface energy approximated by the EPP approach is then obtained by a linear combination of the number of further broken bonds and the EPP parameters:

$$\gamma(hkl) = \sum \boldsymbol{N}_s(hkl)V_s, \tag{4}$$

where $\boldsymbol{N}_s(hkl)$ is the number of sth-nearest broken bonds on the (hkl) surface and V_s is the corresponding effective pair-interaction per bond of sth nearest neighbors, as suggested by Vitos and Moriarty *et al.* [10,16]. This EPP-derived surface energy, in principle, includes these EPP parameters up to the sth nearest neighbors of interest and thus allows us to estimate and predict sufficiently accurate $\gamma(hkl)$.

The EPP parameters can be calculated by solving the simultaneous equations with the surface energy of any surface as input values. In our approach, we have chosen three low-Miller-index surfaces for our EPP model, considering an expansion of up to the third nearest neighbor (i.e., V_1, V_2, and V_3). This ensures not only the accuracy of the prediction, but also the inclusion of the most representative and relevant surfaces in bulk cubic metals.

B. Computational details

All density functional theory (DFT) calculations for the bulk and surface properties of 24 metals (13 bcc metals: Li, Na, K, Rb, Cs, Ba, V, Nb, Ta, Cr, Mo, W, and Fe; 11 fcc metals: Ca, Sr, Rh, Ir, Ni, Pd, Pt, Cu, Ag, Au, and Al) are performed by using the Vienna *ab initio* simulations package (VASP) code [17,18]. A plane-wave basis set with a kinetic-energy cutoff of 500 eV [except for Li (600 eV) and Na (800 eV)] is employed, within the projector augmented-wave (PAW) approach [19]. The generalized gradient approximation to the exchange-correlation functional (GGA) due to Perdew *et al.* (PBEsol) [20] is used, which has been known to perform well for bulk and surface properties of metals.

The Brillouin-zone integrations are performed by using a Γ-centered $\boldsymbol{k}$-point grid with a $\boldsymbol{k}$-spacing method which allows for the smallest spacing of 0.15 Å^{-1} for bulk lattice optimization (for alkali and alkaline-earth metals, a smaller spacing of 0.10 Å^{-1} is used, yielding a denser $\boldsymbol{k}$ mesh). The number of irreducible $\boldsymbol{k}$ points for all metals are reported in Tables S1 and S2 in the Supplemental Material (SM) [21]. The $\boldsymbol{k}$ meshes for all metal surfaces are then scaled according to the surface unit cell dimensions. All DFT calculations for the structural optimization are performed, ensuring the convergence of the total energies and forces on atoms to within 10^{-4} eV and 10^{-3} eV/Å, respectively.

Spin polarization for ferromagnetic metals (Fe and Ni) are explicitly considered. The calculated magnetic moments for Fe and Ni are 2.07 and 0.63 μ_B/atom, respectively. They agree fairly with the reference 2.22 and 0.60 μ_B/atom for Fe and Ni, respectively [22].

Spin-polarized calculations are also performed for all metal atoms, using a 15×15.5×16 Å^3 asymmetric cell. In addition, in order to determine the accurate ground-state configurations of these atoms, Hund's rule is enforced where partial occupancies are prohibited. Namely, only fully occupied or unoccupied states (i.e., 1 or 0) for orbital occupancies are allowed.

In cases of surface calculations, a symmetric slab with an 18 Å vacuum region is used. The thickness of slabs is chosen after carefully testing that the total energy converges to within 1 meV/atom. For the low-Miller-index surfaces of (100), (110), and (111), 13 atomic layers (ALs) have been used. The five innermost layers are fixed to their bulk positions and all other layers are fully relaxed. In order to verify the accuracy of the surface energy calculated by the EPP model, we additionally calculated some selected higher-Miller-index surfaces of both bcc and fcc metals.

TABLE I. Errors in lattice constants a_0, bulk moduli B_0, and cohesive energies E_{coh} of bcc and fcc metals are compared with both experimental (Expt.) and theoretical (Theor.) references [23–26]. MAE stands for mean absolute error (in Å, GPa, and eV/atom, respectively), Max. AE stands for maximum absolute error (in Å, GPa, and eV/atom, respectively), MARE stands for mean absolute relative error (in %), and MRE stands for mean relative error (in %).

	a_0		B_0		E_{coh}	
bcc	Expt.	Theor.	Expt.	Theor.	Expt.	Theor.
MAE	0.04	0.01	22.15	3.22	0.33	0.02
Max. AE	0.10	0.03	121.87	13.44	1.40	0.11
MARE	1.1	0.3	14.4	2.8	7.5	0.5
MRE	− 1.1	0.0	13.9	− 0.1	6.5	0.3
	a_0		B_0		E_{coh}	
fcc	Expt.	Theor.	Expt.	Theor.	Expt.	Theor.
MAE	0.03	0.01	14.74	1.75	0.54	0.04
Max. AE	0.13	0.02	41.27	6.49	1.39	0.09
MARE	0.7	0.2	7.9	1.3	12.1	0.9
MRE	− 0.6	− 0.1	7.3	− 1.1	11.6	0.1

Specifically, for bcc metals, (210), (211), (310), and (321) are selected, while (210), (211), (311), and (331) are chosen for fcc metals. For these high-Miller-index surfaces, a slab model of 19 ALs has been used. All surfaces of (210), (211), (310), and (321) for bcc metals and (210), (211), (311), and (331) for fcc consist of 19 ALs. Here, the five innermost ALs are fixed to their bulk positions while all other layers are fully relaxed. To include the possible influence of high-angled surface steps and kinks on our calculated surface energies, we have also tested much-higher-Miller-index surfaces [namely, (410), (411), (755), and (911) surfaces], which are reported in the SM.

The DFT-derived surface energies γ are calculated based on the equation, $\gamma = (E^{slab} - N^{slab}E^{bulk})/(2A)$, where A is the area of surface structure, E^{slab} is the total DFT energy of the slab system, N^{slab} is the number of metal atoms in the system, and E^{bulk} is the total DFT energy per atom of the metal bulk.

III. RESULTS AND DISCUSSIONS

A. Bulk properties of cubic metals

Bulk properties, such as lattice constant a_0, bulk modulus B_0 (by fitting to the third-order Birch–Murnaghan equation of state [27]), and cohesive energy E_{coh}, of 24 fcc and bcc metals are calculated by using the PBEsol functional. We analyze and present their associated errors, such as mean absolute error (MAE), maximum absolute error (Max. AE), mean absolute relative error (MARE), and mean relative error (MRE) in Table I. The calculated value for each property is then listed in Tables S1 and S2 of the SM. Overall, our calculations show excellent agreement with theoretical reports within 0.01 Å (in lattice constants), 2.55 GPa (in bulk moduli), and 0.03 eV (in cohesive energy) as mean absolute error (MAE), whereas only some cases (e.g., Cr and Fe) show a larger difference with the reported experimental value for B_0 [23–26].

TABLE II. DFT-calculated unrelaxed (γ_{un}) and relaxed (γ_r) surface energies (in units of eV/Å^2) of low-Miller-index surfaces of bcc and fcc metals and the corresponding experimental surface energies (eV/Å^2).

	100		110		111		Ref.
bcc	γ_{un}	γ_r	γ_{un}	γ_r	γ_{un}	γ_r	Expt.
Li	0.030	0.030	0.033	0.033	0.036	0.035	0.033[a]
Na	0.015	0.015	0.014	0.014	0.017	0.017	0.016[a]
K	0.008	0.008	0.007	0.007	0.009	0.009	0.009[a]
Rb	0.006	0.006	0.006	0.006	0.007	0.007	0.007[a]
Cs	0.005	0.005	0.004	0.004	0.006	0.006	0.006[a]
Ba	0.023	0.023	0.023	0.023	0.029	0.028	0.024[a]
V	0.179	0.167	0.170	0.166	0.208	0.186	0.164[a]
Nb	0.177	0.164	0.148	0.145	0.186	0.164	0.169[a]
Ta	0.186	0.171	0.165	0.161	0.211	0.186	0.197[a]
Cr	0.265	0.253	0.227	0.224	0.261	0.243	0.147[a]
Mo	0.236	0.218	0.194	0.189	0.229	0.206	0.187[a]
W	0.285	0.267	0.222	0.218	0.268	0.240	0.230[a]
Fe	0.196	0.195	0.187	0.187	0.210	0.205	0.147[b]
	100		110		111		Ref.
fcc	γ_{un}	γ_r	γ_{un}	γ_r	γ_{un}	γ_r	Expt.
Ca	0.032	0.032	0.037	0.037	0.033	0.032	0.031[a]
Sr	0.024	0.024	0.029	0.029	0.025	0.025	0.026[a]
Rh	0.181	0.177	0.187	0.179	0.154	0.152	0.169[c]
Ir	0.211	0.202	0.219	0.205	0.162	0.160	0.187[c]
Ni	0.164	0.163	0.173	0.169	0.142	0.142	0.149[a]
Pd	0.116	0.115	0.125	0.122	0.099	0.099	0.125[d]
Pt	0.140	0.139	0.152	0.142	0.113	0.113	0.125[e]
Cu	0.114	0.113	0.123	0.120	0.104	0.104	0.114[f]
Ag	0.071	0.071	0.076	0.075	0.067	0.067	0.078[c]
Au	0.074	0.074	0.081	0.077	0.063	0.063	0.094[e]
Al	0.066	0.065	0.072	0.072	0.059	0.058	0.071[e]

[a]Reference [28].
[b]Reference [29].
[c]Reference [30].
[d]Reference [31].
[e]Reference [32].
[f]Reference [1].

B. Surface properties of low-Miller-index surfaces

Having optimized the bulk structure, symmetric slab models of metal surfaces are constructed. We considered both bulk truncated surface models (i.e., no relaxation) as well as those where only a few outermost layers are fully relaxed as written in Methodology. The calculated surface energies of the unrelaxed and relaxed models are listed in Table II and plotted in Fig. 2. The experimentally measured surface energies cannot be directly compared to our results due to isotropic experimental values. However, one can find that our results agree well with experiments generally, since the PBEsol functional was, in part, developed for the purpose of providing a more accurate description of the surface energy [20].

Parabolic trends are observed in Fig. 2, showing a dependence on the d-electron occupation. The metals with half-filled d orbitals show higher surface energies than others, whereas the metals with fully occupied and empty d orbitals exhibit smaller energies [33–36]. The most-close-packed surfaces

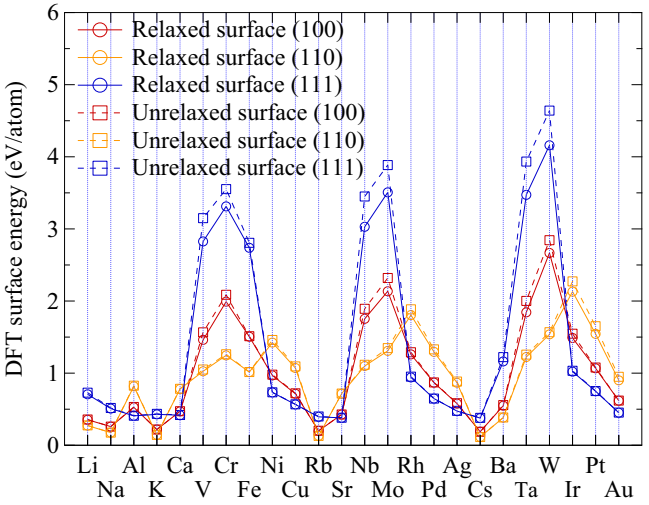

FIG. 2. Comparisons of DFT-calculated surface energies of low-Miller-index surfaces as a function of elements. Red, orange, and blue indicate (100), (110), and (111) surfaces, respectively. Solid lines with circles and dotted lines with squares denote relaxed and unrelaxed surfaces, respectively.

[(110) for bcc and (111) for fcc] are generally the most energetically favorable, which could be rationalized by the broken-bond model [16]. It can also be found that metals with half-filled *d* orbitals and those with a less compact surface tend to exhibit a much larger surface relaxation effect.

To test the influence of spin-orbit coupling (SOC) on surface energies of heavy metals, we considered the low-Miller-index surfaces of two bcc (Mo and W) and fcc metals (Ag and Au). Compared with those without the consideration of SOC, surface energies of Au increase by approximately 3%, while those of W decrease when SOC is explicitly considered. Surface energies of Ag and Mo are not changed when SOC is included, as shown in Table S4 in the SM. Similar observations have been reported in the literature [8,9]. Nevertheless, to verify the effective influence of SOC on the DFT-derived EPP numbers, we checked that the overall trends in the obtained EPP are not changed. Therefore, we neglect the SOC effect in our DFT calculations given that SOC does not significantly affect the surface energy and the EPP parameters of the metals of our interests.

C. Validation of effective pair-potential approach

We obtain the effective pair-potential (EPP) parameters V_1, V_2, and V_3 by solving simultaneous equations of $\gamma(100)$, $\gamma(110)$, and $\gamma(111)$, following Eq. (4). These unique parameters allow us to calculate the surface energy of any plane of interest by taking the number of broken bonds into account. The number of broken bonds, the EPP parameters, as well as the predicted surfaces of some high-Miller-index surfaces are shown in Tables S3 and S5 and in Fig. S1 in the SM, respectively.

In order to verify the accuracy of our results, we also perform a benchmark with DFT surface energies for selected high-Miller-index surfaces. We have chosen four surfaces of four metals for both fcc and bcc, respectively. The chosen

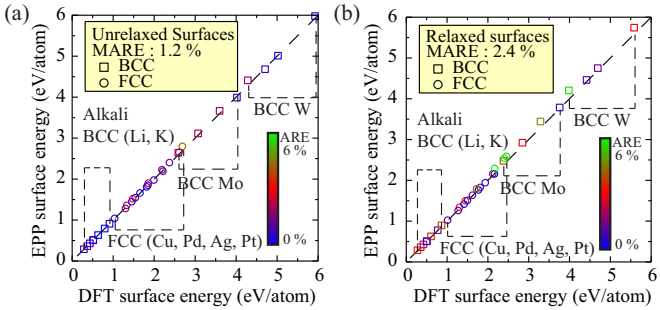

FIG. 3. Surface energy comparisons between DFT and EPP model for selected high-Miller-index surfaces for (a) unrelaxed and (b) relaxed systems. (210), (211), (310), and (321) surfaces for bcc (Li, K, Mo, and W) with squares and (210), (211), (311), and (331) surfaces for fcc (Cu, Pd, Ag, and Pt) with circles are calculated, respectively. Absolute relative errors between DFT and EPP energies are represented by gradient colors. 0%, 3%, and 6% are shown with blue, red, and green, respectively.

surfaces are (210), (211), (310), and (321) of Li, K, Mo, and W for bcc metals and (210), (211), (311), and (331) of Cu, Pd, Ag, and Pt for fcc metals, respectively. The criteria for the choice of surfaces is that these surfaces have the lowest number of broken bonds as compared to the low-Miller-index surfaces. These surfaces are possibly also more relevant due to their relatively lower surface energies. The energy comparisons between DFT and EPP are plotted in Fig. 3 and listed in Table III, while their absolute values are listed in Table S6 in the SM for both the unrelaxed and relaxed surfaces. Overall, our EPP results agree very well with our calculated DFT surface energies. Here, we find that the EPP model shows a much better agreement for unrelaxed surfaces than for relaxed surfaces, i.e., with 1.2% and 2.4% of mean absolute relative error (MARE) for the unrelaxed and relaxed surfaces, respectively. This is easily rationalized by the fact that the broken-bond model is based only on the bond energy in the ideal bulk system. This naturally excludes possible atomic relaxation effects. When it comes to the relaxed surfaces in reality, many surface processes and possible reconstructions will deviate from this simple bond-cutting model. However, we have included the relaxation effect in an average way by employing DFT-derived energies of relaxed surfaces.

TABLE III. Error analysis between the DFT-calculated and EPP-predicted surface energies of selected high-Miller-index surfaces [i.e., (210), (211), (310), and (321) for bcc and (210), (211), (311), and (331) for fcc] for both unrelaxed and relaxed surfaces, respectively. The mean absolute error (MAE) and maximum absolute error (Max. AE) are reported in units of eV/atom and the mean absolute relative error (MARE) and mean relative error (MRE) are given in percent.

	bcc		fcc	
%	Unrelaxed	Relaxed	Unrelaxed	Relaxed
MAE	0.01	0.02	0.02	0.03
Max. AE	0.13	0.22	0.11	0.14
MARE	1.0	2.5	1.4	2.2
MRE	0.4	2.5	0.9	2.1

We consider much-higher-Miller-index surfaces which have a greater number of broken bonds, which allows us to further validate the EPP approach. (410), (411), (755), and (911) planes for bcc Mo and W and fcc Cu and Ag are considered. Mean relative errors of 1.1% and 2.0% for unrelaxed and relaxed surfaces are obtained, respectively. The error is rather similar to that of the surfaces analyzed above. This tells us that the EPP approach would give uniform predictions on higher-Miller-index surfaces. Details of the calculated values are given in Table S7 in the SM.

By using a combination of those low- and high-Miller-index surfaces, we generated two different sets of surface energies as inputs for our EPP model so as to compare their fit results with those obtained by using low-Miller-index surfaces to derive the EPP parameters. Our results are shown in Table S8 in the SM. We notice that these two sets of derived EPP parameters show the same trend as for the low-Miller-index case. However, a larger deviation in the absolute values derived by using the mixed set is evident. We rationalize this deviation as originating from the pressure of steps and kinks in the high-Miller-index surfaces which are absent in the low-Miller-index surfaces. Thus, to promise a higher degree of transferability of the EPP parameters without compromising the reported accuracy, we suggest using the set of low-Miller-index surfaces to determine accurate EPP parameters.

We would also like to take this chance to further comment on the DFT-derived EPP values in Table S5 in the SM. One may notice small and negative values for some V_2 and V_3 parameters. The physics of the bond-cutting model, in principle, demands that all EPP values should be positive. In this work (and also in Ref. [13]), the very small negative values found in the Table S5 in the SM are due to an unphysical artifact from solving these simultaneous linear equations. As seen, these values are generally very close to zero and do not affect our conclusion.

D. Surface energy maps

Successfully validating the accuracy of EPP approach as well as having a full list of EPP parameters for all 24 cubic metals, it becomes fairly trivial to generate the surface energy of any orientation by using Eq. (4). Thus, following the process outlined in Fig. 4, we could provide the "informatics" of surface energies of 24 metals with roughly 32 000 surfaces, encompassing all crystal planes from $\{100\}$ to $\{20\ 20\ 20\}$. Since this large database is able to give us clear trends of surface energetics, as shown in Fig. S2 in the SM, we postprocess it by using various means of visualization techniques, as illustrated below.

We first plot the EPP-derived (relaxed and unrelaxed) surface energy of these metals as a function of relative orientation θ along low-Miller-index planes [i.e., from (100) $\rightarrow$ (111) $\rightarrow$ (110) $\rightarrow$ (100)]. Here, θ is defined as an angle between the surface of interest and of the surface of reference. These $\gamma(\theta)$ plots for the representative fcc metal (Cu) and bcc metal (W) are shown in Figs. 5(a) and 5(b) while that of the remaining 22 metals are shown in Figs. S3, S4, and S5 in the SM. In general, we find that the surface relaxation effects in s metals are less pronounced than in the transition d metals.

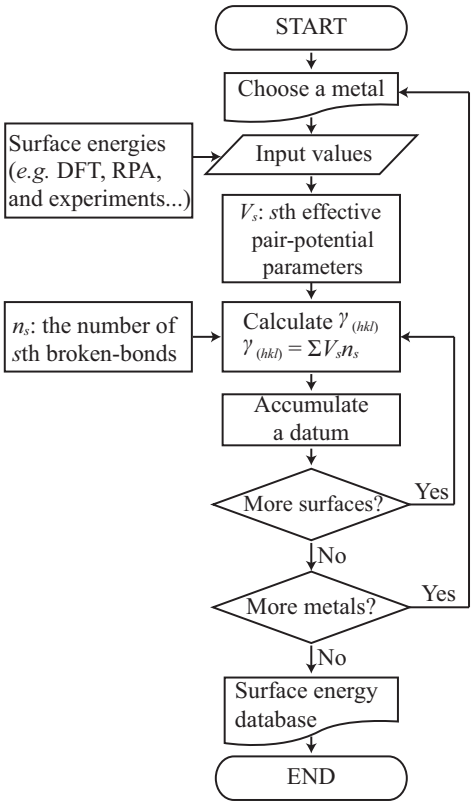

FIG. 4. A flowchart of the effective pair-potential approach to generate the database of surface energies of metal systems.

At first glance, the general dispersion of the surface energy plot agrees well with that reported in the literature [35,37]. The bcc metals exhibit the lowest cusp in the $\gamma(\theta)$ plot for the (110) surface, while fcc metals do so for the (111) surface. Interestingly, a non-negligible lowering of the surface energy is noticed for the (211) surface of bcc metals. For the bcc s metals, $\gamma(211)$ is found to be even lower in energy than $\gamma(111)$ (with the exception of Li), while $\gamma(211)$ is found to be almost similar in energy to $\gamma(111)$ for the bcc d metals. This lowering of the (211) surface energy is also confirmed by DFT calculations. One possible explanation could be attributed to the directionality of the d orbitals in bcc d metals as opposed to the more spherical s orbitals found in the bcc s metals.

Next, we visualize the surface energies via a stereographic projection using the Cartesian coordinates of $\gamma(x,y)$ onto a plane. Following the definition of stereographic projection, the integer Miller index (h,k,l) can be converted to Cartesian coordinates (x,y) in the unit circle by the equation

$$(x,y) = \left(\frac{h}{l+\sqrt{h^2+k^2+l^2}}, \frac{k}{l+\sqrt{h^2+k^2+l^2}}\right). \quad (5)$$

This way of mapping the surface energies leads to a generation of a stereographic net and is commonly termed the "Wulff net" [38,39]. One advantage of the Wulff net is that it allows one to visualize crystallographic planes as points on circular arcs in a circle, thus producing a clear "atlas" of surface energies. Every data point on the Wulff net corresponds to its crystallographic plane (hkl) colored with its EPP-derived surface energy.

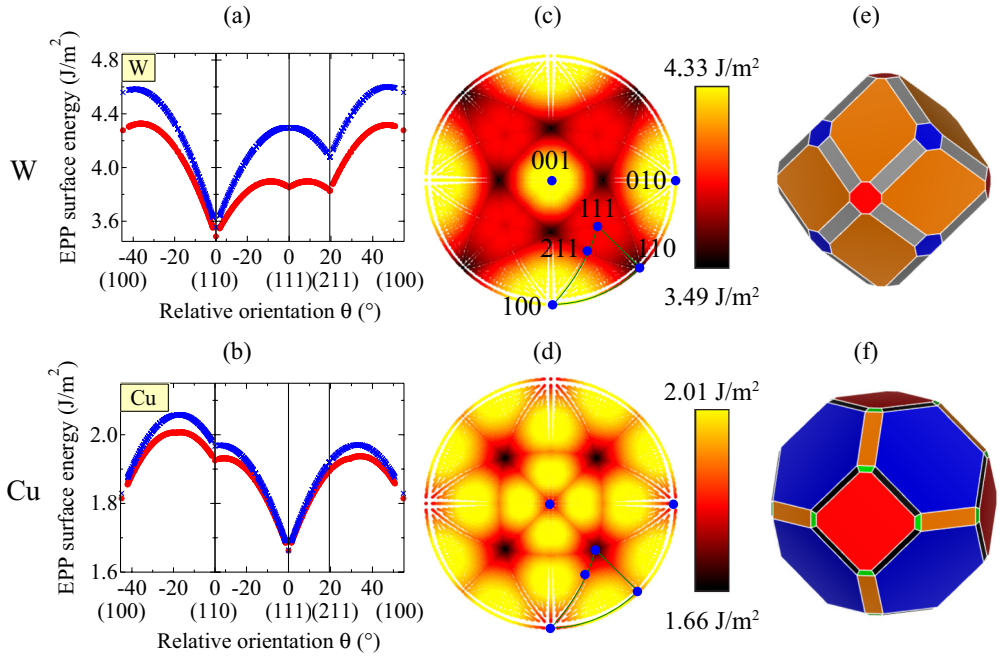

FIG. 5. (a), (b) Surface energies as a function of relative orientation [(100) → (111) → (110) → (100)], (c), (d) Wulff nets made up of surface energies calculated by the EPP model, and (e), (f) predictions of equilibrium crystal shapes (ECSs) are shown for bcc W and fcc Cu. In panels (c) and (d), colors of each point are describing surface energies of the system. High symmetric surfaces are indicated by blue dots. In panel (e) and (f), red, orange, blue, gray, green, and black planes represent (100), (110), (111), (211), (210), and (311), respectively.

The Wulff nets for Cu and W are plotted in Figs. 5(c) and 5(d), respectively (see the SM for all remaining metals). As seen in both Wulff nets, the primary structural boundaries of fcc [i.e., (111) → (100) → (110)] and bcc [i.e., (110) → (211)] are clearly shown. Also, via these stereographic Wulff nets, the relative surface energetics for each element is clearly displayed (i.e., aided by the contrast of colors) for further analysis. In the case of W, the surfaces in the triangular region enclosed by (111), (211), and (110) are energetically more stable than those in the domain surrounded by (100), (211), and (110). On the other hand, for Cu, it can be seen that surfaces near the (111) plane are energetically more favorable.

Thus far, we have expressed the EPP-derived surface energies in two-dimensional plots, either as a function of the orientation angle or as a stereographic projection on a plane. Another popular way to illustrate relative surface energies is to construct a geometrical polyhedron based on the Gibbs–Wulff theorem, yielding the thermodynamic equilibrium crystal shape (ECS) [38,39]. As shown in previous reports, the ECS has been used successfully to predict and explain observed morphologies of nanocrystals [31,40–42]. According to the Gibbs–Wulff theorem, the mathematical construct can be expressed as follows:

$$r(\boldsymbol{d}) = \min\left[\alpha\gamma(\theta)\right]. \tag{6}$$

where $r(\boldsymbol{d})$ represents the radius of the crystal shape in the direction of the vector $\boldsymbol{d}$, and α is a proportionality constant. By the Gibbs–Wulff theorem, one returns to the smallest volume enveloping the origin inside all other crystallographic directions as the thermodynamically most stable morphology for a particular crystal.

Using the EPP-derived surface energies from the surface energy database, and including both low- and high-Miller-index surfaces of the cubic metals considered in this work, we construct the ECS for all 24 metals, showing again only that of Cu and W in Figs. 5(e) and 5(f), respectively. Accordingly, the exposure of high-Miller-index surfaces [e.g., (211) for W and (210) and (311) for Cu] is predicted via EPP-derived ECS for selected metals. It was indeed highlighted in experimental studies that the inclusion of high-Miller-index surfaces for ECS prediction could be crucial, e.g., adsorbate-induced faceting of {112}, {123}, and {178} surfaces in W and Mo systems by Pt and Pd adatoms, and this has been reiterated in recent theoretical works [31,43–45]. From the generated Wulff nets and Wulff polyhedrons, it could be suggested that the high-Miller-index surfaces near the (111) plane of Cu or in the stereographic region along the (111) → (110) → (211) path of W, as shown in Figs. 5(c) and 5(d), is potentially modulated for the benefit of shape-controlled metal-particle synthesis.

E. Case study of Li

Having explained the numerical approach to surface energetics—from data generation to its visualization, using bcc Li as an example—we demonstrate the importance of how the EPP approach can clearly discriminate the strong influence of the second- and third-nearest-neighbor bonds (i.e., V_2 and V_3) on the high-Miller-index surface energetics.

In Fig. 6(a), the primary structural boundaries of bcc [i.e., (110) → (321) → (211)] are found to be barely visible in the Wulff net of Li, in contrast to those in other soft alkali s metals such as K and Rb. Tracing back to the $\gamma(\theta)$ plot of Li, we find that the $\gamma(100)$ of Li is much lower in energy than $\gamma(110)$, unlike most bcc metals where the (110) surface has

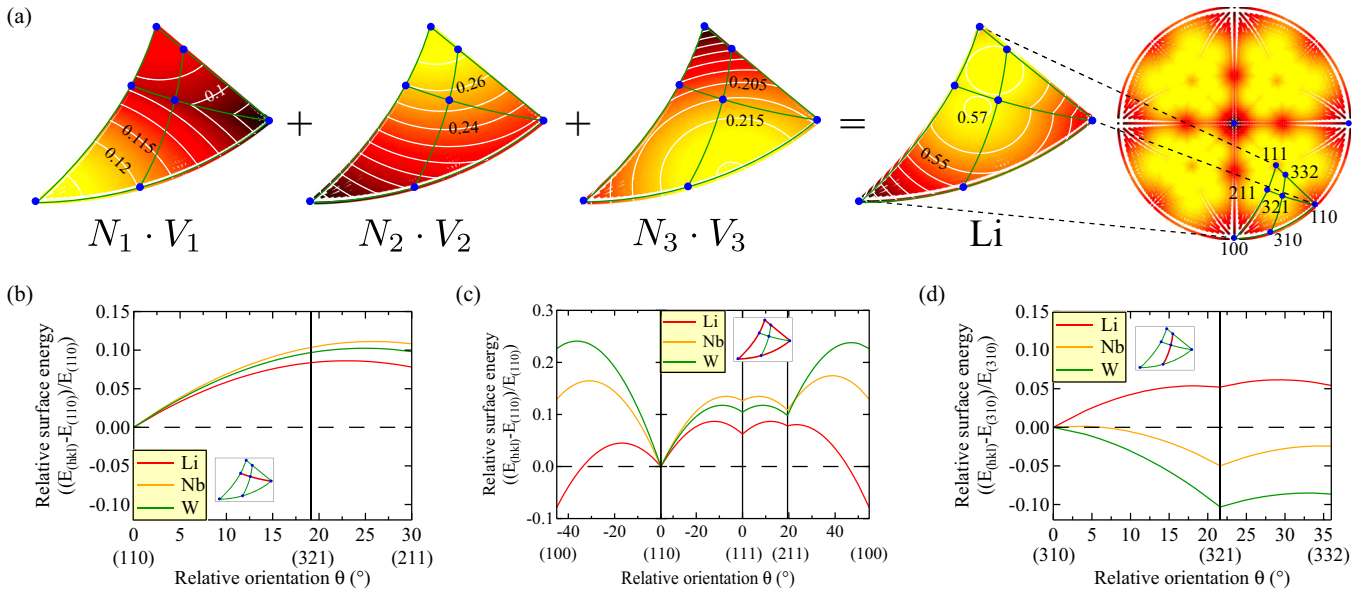

FIG. 6. (a) Wulff net of bcc Li surface energies showing each contribution of first, second, and third nearest-neighbors to surface energy. Representative planes and pathways enclosed by these planes are shown as blue dots and green lines, respectively. The relative surface energies of Li (red), Nb (yellow), and W (green) are shown as functions of relative orientations of the path (b) (110) → (321) → (211), (c) (100) → (110) → (111) → (100), and (d) (310) → (321) → (332), respectively. Paths in panels (b), (c), and (d) are defined by the primary, secondary, and tertiary vectors of bcc, following Ref. [46].

the lowest energy [see Fig. 6(c)]. We stress that both EPP- and DFT-derived surface energies reflect this anomaly. Looking at the EPP parameters of Li, it is found that the V_2 of Li is approximately 2.5 times larger than V_1 (i.e., $V_1 = 23.2$ meV while $V_2 = 58.6$ meV) and, more surprisingly, V_3 works out to be almost 80% that of V_1 (i.e., $V_3 = 18.1$ meV). Similar trends are observed when the different input sets [(100), (210), and (211); (100), (110), and (211)], as shown in Table S10 of the SM. The individual impact of these EPP parameters ($N_s V_s$) has been untangled in Fig. 6(a) to illustrate their contribution to the net surface energy of Li.

By definition, the EPP parameter V_s intrinsically reflects the strength of the effective bond pair interaction of the sth nearest neighbor [10,16]. Utilizing the Wulff net of Li, we traced the relative surface energy variation along different pathways: between (211) and (110) in Fig. 6(b), between (100), (110), and (111) in Fig. 6(c), and between (310) and (332) in Fig. 6(d). The former pathway (211) → (110), which satisfies $h - k - l = 0$, contains the primary surfaces of bcc mainly stabilized by the first-nearest-neighbors bonds, $(1/2)\langle 111\rangle$, while the other pathways [(100) → (110) → (111) and (310) → (332)] contain the secondary and tertiary surfaces by $(1/2)\langle 110\rangle$ and $(1/2)\langle 331\rangle$, respectively, as defined by Jenkins *et al.* [46]. In the primary boundary as shown in Fig. 6(b), one can hardly tell the difference between Li and other bcc metals (e.g., Nb and W). However, when it comes to the secondary and tertiary zones in Figs. 6(c) and 6(d), the relative surface energy variation of Li misses the cusp at (211) and (321) (i.e., intersection boundary with the primary zone), respectively, distinguishing itself from other bcc metals that exhibit a noticeable cusp.

This observed surface energy trend can be explained by the energy cost of cutting these unusually strong second- and third-nearest-neighbor bonds in bulk bcc Li. This accounts for the significant increase in the surface energetics beyond the simple (100) surface, and this physical phenomenon is readily captured by the EPP-derived Wulff net of Li. The importance of this finding leads to the fact that specific primary planes that are meant to be stable in typical bcc metals [i.e., planes near the pathway between (211) and (110)] could become unstable in bcc Li due to the relatively strong interaction of the second- and third-nearest-neighbor bonds. This gives us a clear conclusion that surface energetics of bcc Li cannot be adequately described by merely considering only the first-nearest-neighbor broken bonds nor by the investigations of typical low-Miller-index surfaces.

IV. CONCLUSION

To conclude, we propose a first-principles-based effective pair-potential (EPP) model (beyond the first-nearest-neighbor bond) to generate a surface energy database for a total of 24 cubic fcc and bcc metals. The EPP-derived surface energy database is verified to be within 1% accuracy of DFT calculations. With the database, two-dimensional Wulff nets and three-dimensional Wulff polyhedrons provide an "infographics" of accurate and yet efficient surface energetics to discriminate nearest-neighbor-bond contributions to the overall "surface energy atlas" of these pristine cubic metals. Based on this approach, we have also attempted to interpret an anomaly found in surface energies of bcc Li by analyzing the strong influence of the second- and third-nearest-neighbor bonds to its surface energies. Notwithstanding, it is expected that the EPP-derived surface energy database in this work serves as a good platform to improve the mathematical construct for a more realistic model for real applications, e.g., supported metal nanocatalysts [47,48].

ACKNOWLEDGMENTS

We gratefully acknowledge support from the Basic Science Research Program by the National Research Foundation of Korea (NRF-2014R1A1A1003415) and the Australian Research Council (ARC). This work was also supported by the third Stage of Brain Korea 21 Plus Project Division of Creative Materials. Computational resources have been provided by the National Computational Infrastructure (NCI), which is supported by the Australian Government, and by Korea Institute of Science and Technology Information (KISTI) supercomputing centre (KSC-2015-C3-030). We thank S. M. Kim for his contribution to the graphical abstract.

[1] J. L. F. Da Silva, C. Stampfl, and M. Scheffler, Surf. Sci. **600**, 703 (2006).
[2] D. K. Yu, H. P. Bonzel, and M. Scheffler, New J. Phys. **8**, 65 (2006).
[3] C. Fiolhais and L. M. Almeida, Int. J. Quantum Chem. **101**, 645 (2005).
[4] J. M. Pitarke and J. P. Perdew, Phys. Rev. B **67**, 045101 (2003).
[5] L. A. Constantin, J. M. Pitarke, J. F. Dobson, A. Garcia-Lekue, and J. P. Perdew, Phys. Rev. Lett. **100**, 036401 (2008).
[6] Q. Jiang, H. M. Lu, and M. Zhao, J. Phys.: Condens. Matter **16**, 521 (2004).
[7] M. C. Desjonquères and D. Spanjaard, *Concepts in Surface Physics*, 2nd ed. (Springer-Verlag, Berlin, 1998).
[8] I. Galanakis, G. Bihlmayer, V. Bellini, N. Papanikolaou, R. Zeller, S. Blügel, and P. H. Dederichs, Europhys. Lett. **58**, 751 (2002).
[9] I. Galanakis, N. Papanikolaou, and P. H. Dederichs, Surf. Sci. **511**, 1 (2002).
[10] L. Vitos, H. L. Skriver, and J. Kollár, Surf. Sci. **425**, 212 (1999).
[11] M. W. Finnis and J. E. Sinclair, Philos. Mag. A **50**, 45 (1984).
[12] S. Wei and M. Y. Chou, Phys. Rev. B **50**, 4859 (1994).
[13] J. L. F. Da Silva, C. Barreteau, K. Schroeder, and S. Blügel, Phys. Rev. B **73**, 125402 (2006).
[14] Z. Yu and A. Flodström, Surf. Sci. **401**, 236 (1998).
[15] J. K. Mackenzie, A. J. Moore, and J. F. Nicholas, J. Phys. Chem. Solids **23**, 185 (1962).
[16] J. A. Moriarty and R. Phillips, Phys. Rev. Lett. **66**, 3036 (1991).
[17] G. Kresse and J. Hafner, Phys. Rev. B **47**, 558 (1993).
[18] G. Kresse and J. Furthmüller, Phys. Rev. B **54**, 11169 (1996).
[19] G. Kresse and D. Joubert, Phys. Rev. B **59**, 1758 (1999).
[20] J. P. Perdew, A. Ruzsinszky, G. I. Csonka, O. A. Vydrov, G. E. Scuseria, L. A. Constantin, X. Zhou, and K. Burke, Phys. Rev. Lett. **100**, 136406 (2008).
[21] See Supplemental Material at http://link.aps.org/supplemental/10.1103/PhysRevB.93.035434 for the computational details in higher-Miller-index surfaces calculations, additional results, and the details of validation of EPP approach.
[22] B. D. Cullity and C. D. Grahm, *Introduction to Magnetic Materials* (John Wiley & Sons, Inc., Hoboken, 2009).
[23] G. I. Csonka, J. P. Perdew, A. Ruzsinszky, P. H. T. Philipsen, S. Lebègue, J. Paier, O. A. Vydrov, and J. G. Ángyán, Phys. Rev. B **79**, 155107 (2009).
[24] L. Schimka, R. Gaudoin, J. Klimeš, M. Marsman, and G. Kresse, Phys. Rev. B **87**, 214102 (2013).
[25] P. Janthon, S. M. Kozlov, F. Viñes, J. Limtrakul, and F. Illas, J. Chem. Theory Comput. **9**, 1631 (2013).
[26] A. D. Corso, J. Phys.: Condens. Matter **25**, 145401 (2013).
[27] F. Birch, Phys. Rev. **71**, 809 (1947).
[28] W. R. Tyson and W. A. Miller, Surf. Sci. **62**, 267 (1977).
[29] A. Dannenberg, M. E. Gruner, A. Hucht, and P. Entel, Phys. Rev. B **80**, 245438 (2009).
[30] F. R. de Boer, R. Boom, W. C. M. Mattens, A. R. Miedema, and A. K. Niessen, *Cohesion in Metals: Transition Metal Alloys Cohesion and Structure* (Amsterdam, North Holland, 1989).
[31] S.-H. Yoo, J.-H. Lee, B. Delley, and A. Soon, Phys. Chem. Chem. Phys. **16**, 18570 (2014).
[32] N. E. Singh-Miller and N. Marzari, Phys. Rev. B **80**, 235407 (2009).
[33] J.-M. Albina, C. Elsässer, J. Weissmüller, P. Gumbsch, and Y. Umeno, Phys. Rev. B **85**, 125118 (2012).
[34] L. Vitos, A. V. Ruban, H. L. Skriver, and J. Kollár, Surf. Sci. **411**, 186 (1998).
[35] M. Methfessel, D. Hennig, and M. Scheffler, Appl. Phys. A: Solids Surf. **55**, 442 (1992).
[36] H. L. Skriver and N. M. Rosengaard, Phys. Rev. B **46**, 7157 (1992).
[37] M. Methfessel, D. Hennig, and M. Scheffler, Phys. Rev. B **46**, 4816 (1992).
[38] G. Wulff, Z. Kristallogr. - Cryst. Mater. **34**, 449 (1901).
[39] G. Wulff, Z. Kristallogr. - Cryst. Mater. **36**, 1 (1902).
[40] A. Soon, M. Todorova, B. Delley, and C. Stampfl, Phys. Rev. B **75**, 125420 (2007).
[41] X. Duan, O. Warschkow, A. Soon, B. Delley, and C. Stampfl, Phys. Rev. B **81**, 075430 (2010).
[42] T. Lee, B. Delley, C. Stampfl, and A. Soon, Nanoscale **4**, 5183 (2012).
[43] G. Antczak, T. E. Madey, M. Błaszczyszyn, and R. Błaszczyszyn, Vacuum **63**, 43 (2001).
[44] Y.-W. Liao, L. H. Chen, K. C. Kao, C.-H. Nien, M.-T. Lin, and K.-J. Song, Phys. Rev. B **75**, 125428 (2007).
[45] A. Soon, X.-Y. Cui, B. Delley, S.-H. Wei, and C. Stampfl, Phys. Rev. B **79**, 035205 (2009).
[46] S. J. Jenkins and S. J. Pratt, Surf. Sci. Rep. **62**, 373 (2007).
[47] S. Yang, D. Y. Chung, Y.-J. Tak, J. Kim, H. Han, J.-S. Yu, A. Soon, Y.-E. Sung, and H. Lee, Appl. Catal., B **174**, 35 (2015).
[48] Y. J. Tak, W. Jang, N. A. Richter, and A. Soon, Phys. Chem. Chem. Phys. **17**, 9680 (2015).